

## Article

# Si<sub>3</sub>N<sub>4</sub>-Assisted Densification Sintering of Na<sub>3</sub>Zr<sub>2</sub>Si<sub>2</sub>PO<sub>12</sub> Ceramic Electrolyte toward Solid-State Sodium Metal Batteries

Wenwen Sun, Yang Li, Chen Sun, Zheng Sun, Haibo Jin and Yongjie Zhao \* 

Beijing Key Laboratory of Construction Tailorable Advanced Functional Materials and Green Applications, School of Materials Science and Engineering, Beijing Institute of Technology, Beijing 100081, China

\* Correspondence: zhaoyj14@bit.edu.cn

**Abstract:** The solid-state metal battery with solid-state electrolytes has been considered the next generation of energy storage technology owing to its superior safety and high energy density. But, unfavorable ionic conductivity and interfacial problems make it difficult to widely use in practice. In this work, Si<sub>3</sub>N<sub>4</sub> was rationally introduced into the NASICON matrix as a sintering aid, and the influence of Si<sub>3</sub>N<sub>4</sub> on the crystal phase, microstructure, electrochemical and electrical performance of Na<sub>3</sub>Zr<sub>2</sub>Si<sub>2</sub>PO<sub>12</sub> (NZSP) ceramic was systematically studied. The results demonstrate that the introduction of Si<sub>3</sub>N<sub>4</sub> can effectively lower the densification sintering temperature of Na<sub>3</sub>Zr<sub>2</sub>Si<sub>2</sub>PO<sub>12</sub> electrolyte and enhance the room temperature ionic conductivity of the NZSP to  $3.82 \times 10^{-4}$  S cm<sup>-1</sup>. In addition, since Si<sub>3</sub>N<sub>4</sub> has a high thermal conductivity and can inhibit the transmission of electrons between the grains of the electrolyte matrix, it will effectively hinder the generation of sodium metal dendrites and relieve the concentration of the heat source. Moreover, owing to the desirable interface compatibility of the Na and NZSP-Si<sub>3</sub>N<sub>4</sub> electrolyte, the Na/NZSP-1150-1%Si<sub>3</sub>N<sub>4</sub>/Na symmetric battery exhibits excellent stability, and the electrode/electrolyte interface still maintains good integrity even after long-term cycling. The assembled Na/NZSP-1150-1%Si<sub>3</sub>N<sub>4</sub>/Na<sub>3.5</sub>V<sub>0.5</sub>Mn<sub>0.5</sub>Fe<sub>0.5</sub>Ti<sub>0.5</sub>(PO<sub>4</sub>)<sub>3</sub> cell manifests an initial specific capacity of 152.5 mA h g<sup>-1</sup>, together with an initial Coulombic efficiency of 99.8%. Furthermore, after 200 cycles, the battery displays a capacity retention rate of 82%.



**Citation:** Sun, W.; Li, Y.; Sun, C.; Sun, Z.; Jin, H.; Zhao, Y. Si<sub>3</sub>N<sub>4</sub>-Assisted Densification Sintering of Na<sub>3</sub>Zr<sub>2</sub>Si<sub>2</sub>PO<sub>12</sub> Ceramic Electrolyte toward Solid-State Sodium Metal Batteries. *Batteries* **2024**, *10*, 359. <https://doi.org/10.3390/batteries10100359>

Academic Editor: Alejandro Varez

Received: 6 September 2024

Revised: 29 September 2024

Accepted: 8 October 2024

Published: 11 October 2024



**Copyright:** © 2024 by the authors. Licensee MDPI, Basel, Switzerland. This article is an open access article distributed under the terms and conditions of the Creative Commons Attribution (CC BY) license (<https://creativecommons.org/licenses/by/4.0/>).

**Keywords:** NASICON; Si<sub>3</sub>N<sub>4</sub>; solid-state sodium metal battery; interfacial compatibility

## 1. Introduction

The electrochemical energy storage system has drawn considerable attention due to its easy maintenance requirements and great energy conversion efficiency. At present, lithium-ion batteries (LIBs) occupy most of the application market. However, because lithium resources are limited in reserves on earth, it forced researchers to develop a potential lithium-alternative battery system. On account of the high natural reserves of Na and high safety, sodium-ion batteries (SIBs) are considered a hopeful substitute for LIBs [1–6]. But, there are still some safety challenges for SIBs with organic liquid electrolytes, such as leakage and flammability. Solid-state electrolytes (SSE) can solve the aforementioned safety issues while simultaneously enabling the development of high-energy density systems in conjunction with metallic sodium anodes and sodium-ion cathodes that exhibit high operating potentials and specific capacities.

NASICON-type Na<sub>1+x</sub>Zr<sub>2</sub>Si<sub>x</sub>P<sub>3-x</sub>O<sub>12</sub> (0 ≤ x ≤ 3) has become popular worldwide because of its low electronic conductivity, excellent mechanical properties, and favorable chemical and thermal stability. The NASICON-type ceramic electrolyte has an ionic conductivity of about 10<sup>-4</sup> S cm<sup>-1</sup> at room temperature when x = 2 (Na<sub>3</sub>Zr<sub>2</sub>Si<sub>2</sub>PO<sub>12</sub>, abbreviated as NZSP). High-temperature solid-state reaction is one of the most commonly used approaches for the preparation of NZSP ceramic electrolyte, with sintering temperatures for high degree densification usually exceeding 1200 °C. This process often results in the formation of certain impurity phases at the grain boundary due to the volatilization of

some elements such as P and Na [7–9]. Furthermore, the high interfacial impedance and inadequate interfacial compatibility between solid electrodes and SSEs represent two significant long-term obstacles to the universal application of solid metal batteries, which are closely related to the microstructure and composition of the interface. In addition, the high electronic conductivity of SSEs means that metal dendrites are prone to generate within the solid electrolytes [10–12]. On the other hand, due to the heterogeneous plating/stripping of sodium ions during the battery cycling process, inhomogeneous thermal distributions and hot spots are generated within solid electrolytes, wherein promoted growth of metallic sodium dendrites would be accelerated [13]. Accordingly, the formation and further development of metal dendrites endow a significant negative influence on the solid-state batteries' performance.

Silicon nitride ( $\text{Si}_3\text{N}_4$ ) is an insulating material possessing high theoretical thermal conductivity ( $320 \text{ W m}^{-1} \text{ K}^{-1}$ ), and its electronic conductivity is usually lower than  $10^{-12} \text{ S cm}^{-1}$ , which is 4–5 orders of magnitude lower compared to NZSP ceramic electrolytes [14–17]. Based on the above advantages, it is assumed that if  $\text{Si}_3\text{N}_4$  is used as a sintering additive for NZSP ceramics, it can lower the electronic conductivity of the matrix and enhance the thermal conductivity. Furthermore, because the O element is more electronegative than N, the bond energy of Na-O should be much higher than that of Na-N, implying that Na-N could be easier to form [18–20]. Therefore, the interfacial compatibility between the  $\text{Si}_3\text{N}_4$ -modified NZSP ceramic electrolyte and Na metal will be improved.

As a result,  $\text{Na}_3\text{Zr}_2\text{Si}_2\text{PO}_{12}-x\text{Si}_3\text{N}_4$  ceramic electrolytes were synthesized by high-temperature solid reaction. The results exhibit that adding  $\text{Si}_3\text{N}_4$  could increase the densification of the matrix and increase the intergranular force, well improving the ion transport of the NZSP ceramic electrolyte. Meanwhile, the electronic conductivity of the ceramic electrolyte reduces, coupled with the good thermal conductivity of  $\text{Si}_3\text{N}_4$ , and the generation of solid metal dendrites at the solid electrode/electrolyte is significantly suppressed. Furthermore, the wettability between NZSP- $\text{Si}_3\text{N}_4$  and Na metal is significantly improved and a low interface contact resistance of  $17 \Omega \text{ cm}^2$  is obtained. Demonstrating the superior capabilities of the NZSP- $x\text{Si}_3\text{N}_4$  ceramic electrolyte, the assembled solid-state battery exhibits promising electrochemical performance and room-temperature cycling stability.

## 2. Experimental Section

### 2.1. Synthesis of $\text{Na}_3\text{Zr}_2\text{Si}_2\text{PO}_{12}-x\text{Si}_3\text{N}_4$ Ceramics

The conventional solid-state reaction was used to synthesize  $\text{Na}_3\text{Zr}_2\text{Si}_2\text{PO}_{12}-x\text{Si}_3\text{N}_4$  (abbreviated as NZSP- $x\text{Si}_3\text{N}_4$ ,  $x = 0, 1, 3, 5$  and  $7 \text{ wt.\%}$ ). The raw materials consisted of  $\text{Na}_2\text{CO}_3$  (99.5%),  $\text{SiO}_2$  (99.5%),  $\text{ZrO}_2$  (99.99%) and  $\text{NH}_4\text{H}_2\text{PO}_4$  (99.0%). Since the high-temperature sintering process causes volatilization of Na elemental, an excess of  $\text{Na}_2\text{CO}_3$  (10 wt.%) was added for compensation. After weighing these untreated raw materials in accordance with the initially proposed molar ratio, the mixture was thoroughly ball-milled with anhydrous ethanol as the grinding medium. Upon completion, we poured out the slurry and placed it in an electric oven to dry. Then, we placed the powder in a muffle furnace for pre-calcination at  $1000 \text{ }^\circ\text{C}/10 \text{ h}$  (with a heating rate of  $5 \text{ }^\circ\text{C min}^{-1}$ ). Then, different weights of  $\text{Si}_3\text{N}_4$  (0, 1, 3, 5 and 7 wt.%) were added to the as-obtained product, which was then ball-milled again. After drying, pellets were prepared with a size of 10 mm in diameter under 10 MPa and then sintered at  $1150$  and  $1200 \text{ }^\circ\text{C}$  for 10 h. The as-sintered ceramic electrolyte had a diameter of 8–9 mm and a thickness of about 1 mm. Finally, we used sandpaper to polish the ceramic electrolytes before use.

### 2.2. Material Characterization

Powder X-ray diffraction (Rigaku SmartLab, Cedar Park, TX, USA) was utilized to examine the phase structure of the synthesized ceramic electrolytes. Scanning Electron Microscopy (Hitachi Regulus-8230, Tokyo, Japan) was utilized to study the composition and microstructure of the ceramic electrolytes. XPS (X-ray photoelectron spectroscopy) analysis was used to explore the elements' chemical bonding state.

The equation  $\sigma = L/(R \times S_1)$  was applied to compute the ionic conductivity ( $\sigma_t$ ) of the synthesized samples, wherein  $L$  is the thickness,  $R$  is the resistance of the sample and  $S_1$  is the area. To verify the activation energy of ion transfer,  $\sigma_T = A \exp(-E_a/kT)$  was employed, where  $A$  is the pre-exponential factor,  $\sigma$  is the ionic conductivity at a specific temperature,  $k$  is Boltzmann's constant and  $E_a$  is the ion transfer activation energy. ASR =  $R_{\text{interface}} \times S_2$  was used to calculate the interfacial area specific resistance, where  $R_{\text{interface}}$  is the interfacial resistance and  $S_2$  is the contact area of the electrode/electrolyte interface.

Direct current (DC) polarization was used to determine the electronic conductivity through an electrochemical workstation, where the voltage was 1 V. To obtain the electron conductivity of the synthesized ceramic electrolytes, Ohm's law  $\sigma_e = IL/US_3$  was utilized, wherein  $I$  is the current of steady state,  $U$  is the external voltage,  $L$  is the distance to the gold electrode, and  $S_3$  is the area of the charge carriers during their migration.

### 2.3. Electrochemical Performance Evaluation

In a glove box with Ar gas, symmetric sodium metal batteries of CR2032 type were assembled to examine the electrochemical properties of ceramic electrolytes. Sodium metal was pressed (area ~0.3 cm<sup>2</sup>) on both sides of the electrolyte.

Solid-state sodium metal full cells were constructed in CR2032 type. The cathode active material used Na<sub>3.5</sub>V<sub>0.5</sub>Mn<sub>0.5</sub>Fe<sub>0.5</sub>Ti<sub>0.5</sub>(PO<sub>4</sub>)<sub>3</sub> (Me-NVMP), and the anode applied Na foil and solid electrolyte employed NZSP-1150-1%Si<sub>3</sub>N<sub>4</sub> ceramic. The working cathode was generated by mixing Me-NVMP, carbon black and poly (vinylidene difluoride) in a weight ratio of 7:2:1, with NMP (N-methyl-2-pyrrolidinedione) as a solvent. As-obtained slurry was cast on an aluminum foil and vacuum dried at 80 °C. It was then perforated into disks with a loading of about 2 mg cm<sup>-2</sup>. To minimize the interfacial impedance of the composite cathode/solid electrolyte interface, 10 µL of organic liquid electrolyte (1 M NaClO<sub>4</sub> in EC:PC (1:1) solution containing 5% FEC) was used. The NEWARE Battery Testing System (CT-4008Tn-5V10mA-HWX, Shenzhen, China) was used to assess the electrochemical performance.

## 3. Results and Discussion

The phase structure of these samples was assessed using XRD. Figures 1a and S1 show the collected XRD patterns of Na<sub>3</sub>Zr<sub>2</sub>Si<sub>2</sub>PO<sub>12</sub>-xSi<sub>3</sub>N<sub>4</sub>. The diffraction patterns exhibit characteristic peaks that are consistent with the reference pattern of Na<sub>3</sub>Zr<sub>2</sub>Si<sub>2</sub>PO<sub>12</sub> (PDF#01-070-0234). This observation suggests that the incorporation of Si<sub>3</sub>N<sub>4</sub> could not change the crystal structure of the NZSP. Furthermore, diffraction peaks of the ZrO<sub>2</sub> phase are observed in the XRD patterns, which are attributed to the high-temperature volatilization of the P and Na [9,21]. In addition, no diffraction peaks of the additional phases can be observed. For the sake of investigating the influence of Si<sub>3</sub>N<sub>4</sub> on the morphology of Na<sub>3</sub>Zr<sub>2</sub>Si<sub>2</sub>PO<sub>12</sub> ceramic electrolyte, Scanning Electron Microscopy (SEM) was carried out on NZSP-1150-xSi<sub>3</sub>N<sub>4</sub> samples, as shown in Figure 1b, and the cross-sectional SEM image of NZSP-1200 is exhibited in Figure S2. The results demonstrate that the pure NZSP exhibits distinct grain boundaries and some pores. Furthermore, abnormal grain growth can be observed, and the intergranular fracture morphology suggests a deficiency in the strength of the grain–grain bonding [22]. In contrast, the NZSP-1150-1%Si<sub>3</sub>N<sub>4</sub> presents larger grain sizes, fewer pores, and exhibits a much denser microstructure. It can be further observed that the incorporation of Si<sub>3</sub>N<sub>4</sub> can effectively depress the grain abnormal growth, keep the grain size uniform, and reduce the voids among grains, hence promoting a more compact grain contact. Meanwhile, with increasing the content of Si<sub>3</sub>N<sub>4</sub>, it can be noticed that the grains gradually become smaller, and the grain boundaries become more ambiguous. Additionally, the fracture behavior of the ceramics undergoes a transformation, shifting from intergranular to transcrystalline fracture. This observation suggests the presence of stronger grain bonding [23]. Therefore, it can be concluded that a dense microstructure of Si<sub>3</sub>N<sub>4</sub>-modified NZSP ceramics can be obtained at a relatively lower sintering temperature, suggesting that the intergranular phase could lower the densification sintering temperature.

of the NASICON. Furthermore, the results of the EDS mapping show a uniform dispersion of the elements (Figure 1c).

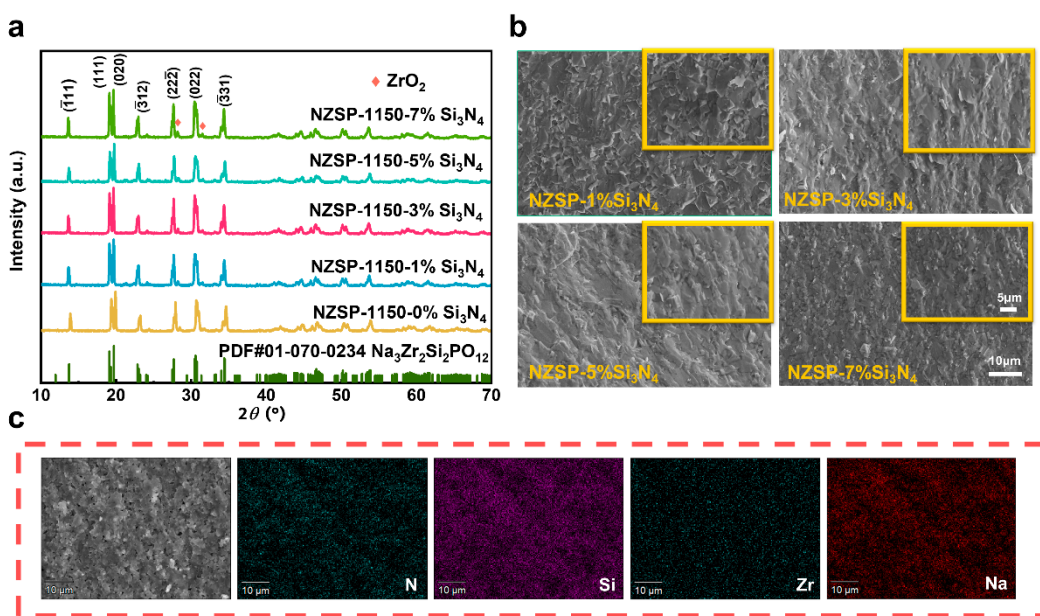


**Figure 1.** (a) XRD patterns of NZSP-1150- $x$ Si<sub>3</sub>N<sub>4</sub>. (b) Cross-sectional SEM images of NZSP-1150- $x$ Si<sub>3</sub>N<sub>4</sub>. (c) EDS mapping results of NZSP-1150-1%Si<sub>3</sub>N<sub>4</sub>.

To evaluate the influence of Si<sub>3</sub>N<sub>4</sub> on the NZSP, an electrochemical impedance spectroscopy (EIS) test was conducted, as illustrated in Figure 2a and Figure S3. It can be observed that the EIS plot shows a sloping line at a low-frequency region and a semicircle at a high-frequency region. As illustrated in Figure S4, the intercept of the semicircle represents the total electrical ( $R_t$ ), while the diameter of the semicircle is indicative of the grain boundary resistance ( $R_{gb}$ ) [24,25]. Therefore, it can be generalized that the impedance of the samples at different sintering temperatures tends to decrease first and subsequently increase with the increasing content of Si<sub>3</sub>N<sub>4</sub>. After that, the total ionic conductivity was computed according to the measured resistance, as shown in Figure 2b and Table S1. In general, the trend in ionic conductivity with the addition of Si<sub>3</sub>N<sub>4</sub> corresponds to the trend in impedance (Figure 2a). Specifically, the ionic conductivity of NZSP-1150- $x$ Si<sub>3</sub>N<sub>4</sub> ( $x = 1\%, 3\%$ ) is much better than that of NZSP-1150 ( $2.04 \times 10^{-4} \text{ S cm}^{-1}$ ), and even higher than NZSP-1200 ( $3.48 \times 10^{-4} \text{ S cm}^{-1}$ ). NZSP-1150-1% Si<sub>3</sub>N<sub>4</sub> in particular achieves the highest ionic conductivity ( $3.82 \times 10^{-4} \text{ S cm}^{-1}$ ) among all samples (Table S1). In other words, compared to pure NZSP sintered at 1200 °C, Si<sub>3</sub>N<sub>4</sub>-modified NZSP ceramics can be sintered at lower sintering temperatures while achieving higher room-temperature ionic conductivity. However, the ionic conductivity of NZSP- $x$ Si<sub>3</sub>N<sub>4</sub> would become decreased when the content of Si<sub>3</sub>N<sub>4</sub> continues to increase. This phenomenon can be well explained by the SEM analysis results of these ceramic electrolytes. This is because  $R_{gb}$  is the major factor for the total ionic conductivity of NASICON electrolytes. When an appropriate amount of Si<sub>3</sub>N<sub>4</sub> is introduced, the average grain size of the matrix is larger, the particles are more tightly connected, and the microstructure of the matrix becomes denser, reducing the  $R_{gb}$ , and ultimately promoting the total ionic conductivity [26–29]. Nevertheless, when the content of Si<sub>3</sub>N<sub>4</sub> is in excess, the increase in grain boundary concentration because of the decrease in the average grain size, together with the overly tight intergranular bonding, leads to excessive grain boundary density, ultimately causing tough ion migration and a decrease in the total ionic conductivity. Meantime, the different temperature EIS of the ceramic electrolytes were collected and the ionic migration activating energy was calculated. Figures 2c,d and S5 display the Nyquist plots for NZSP-1150, NZSP-1150-

1% $\text{Si}_3\text{N}_4$ , and NZSP-1200 at 35–65 °C. The inserts show the Arrhenius plots of the ionic conductivity of these samples as the function of temperature, calculated to be 0.39, 0.37 and 0.38 eV, respectively. It is reconfirmed that introducing  $\text{Si}_3\text{N}_4$  can reduce the barrier of  $\text{Na}^+$  migration.

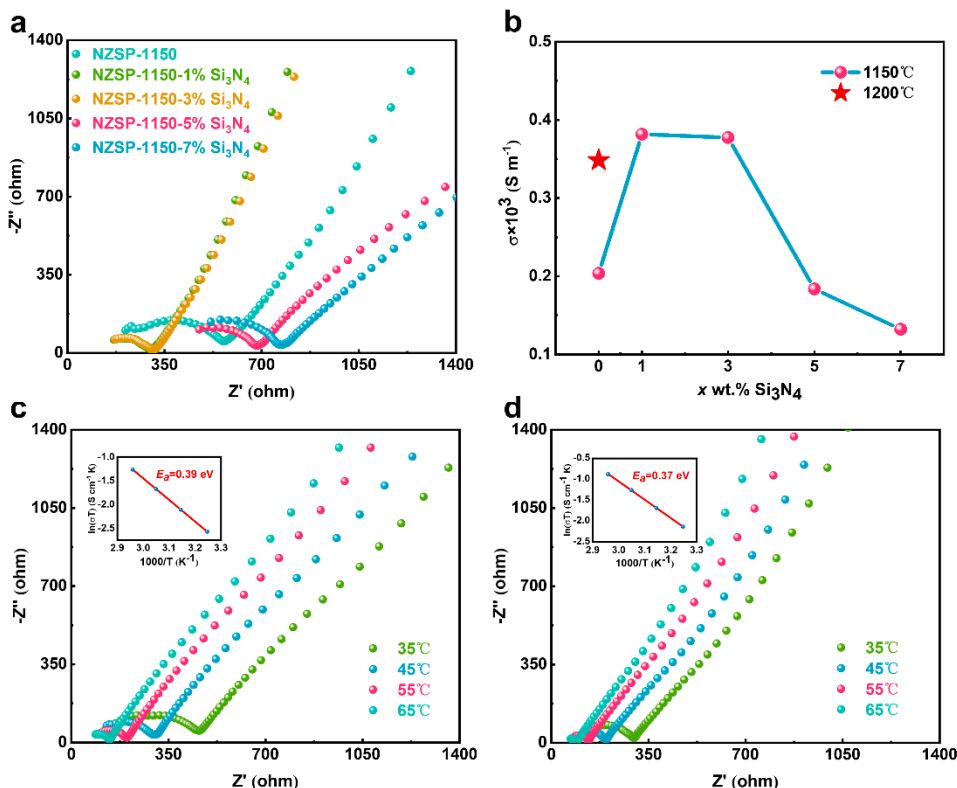


**Figure 2.** (a) Electrochemical impedance spectra of NZSP-1150- $x\text{Si}_3\text{N}_4$ . (b) Ionic conductivity of NZSP-1150- $x\text{Si}_3\text{N}_4$  and NZSP-1200 at room temperature. Total ionic conductivity variation and Nyquist plots variation with the temperature of (c) NZSP-1150 and (d) NZSP-1150-1% $\text{Si}_3\text{N}_4$ .

To assess the interface compatibility between the metallic Na electrode and solid electrolyte, symmetric Na metal batteries were assembled with NZSP-1150 and NZSP-1150-1% $\text{Si}_3\text{N}_4$  as the solid electrolytes. The wettability of the two kinds of ceramic electrolytes against sodium metal was first tested (Figure 3a). It is demonstrated that the wetting angle of NZSP-1150-1% $\text{Si}_3\text{N}_4$  is obviously smaller than that of NZSP-1150. This is because of the weaker electronegativity of N compared to elemental O. Therefore, the N-Na bonding energy is lower and easier to form [18–20]. As a result, the interfacial bonding between the  $\text{Si}_3\text{N}_4$ -doped NZSP electrolyte and the sodium metal is much tighter, allowing for improved interfacial compatibility. The EIS plots of the assembled symmetric Na metal batteries are shown in Figure 3b, and the inset shows the interfacial area specific resistance (ASR). Figure S6 displays the Nyquist plot using the equivalent circuit, wherein the resistance consists of the interfacial contact resistance and the solid electrolyte impedance. The resistance of the Na/NZSP-1150-1% $\text{Si}_3\text{N}_4$ /Na is much smaller than that of the Na/NZSP-1150/Na. Further, the symmetric Na battery with pure NZSP has an ASR of 106  $\Omega$  cm<sup>2</sup>. In contrast, the ASR of Na/NZSP-1150-1% $\text{Si}_3\text{N}_4$ /Na is only 17  $\Omega$  cm<sup>2</sup>, indicating that the  $\text{Si}_3\text{N}_4$  at the grain boundary could effectively improve the electrode/electrolyte interfacial contact, which also corresponds to the previous wettability test. In order to assess the solid electrolyte's capability to resist metal dendrites, the critical current densities of the two cells were tested. In Figure 3c,d, the current density is increased in increments of 0.05 mA cm<sup>-2</sup>, and the Na/NZSP-1150/Na fails at 0.75 mA cm<sup>-2</sup>. The Na/NZSP-1150-1% $\text{Si}_3\text{N}_4$ /Na cell fails at 1.15 mA cm<sup>-2</sup>, which is attributed to the increased density of

the ceramic with improved mechanical behavior and resistance capability against metal dendrite [30,31]. Subsequently, galvanostatic discharge/charge tests were conducted. As illustrated in Figure 3e, at room temperature the Na/NZSP-1150/Na can stably cycle at  $0.05 \text{ mA cm}^{-2}$  for 200 h, but when the current density is elevated to  $0.1 \text{ mA cm}^{-2}$ , the polarization curve becomes asymmetric, indicating that the plating/stripping of Na ions is uneven. Consequently, as the cycle time increases, the battery short-circuits at about 330 h. On the contrary, Figure 3f shows that Na/NZSP-1150-1% $\text{Si}_3\text{N}_4$ /Na can cycle stably for 200 h at both  $0.05$  and  $0.1 \text{ mA cm}^{-2}$ , and can still work well even at  $0.15 \text{ mA cm}^{-2}$  without any significant change in the polarization response, indicating that  $\text{Na}^+$  can be uniformly plating/stripping at the interface, effectively inhibiting sodium metal dendrites growth. Therefore, the higher critical current density and good rate performance of the NZSP-1150-1% $\text{Si}_3\text{N}_4$  battery are assigned to the enhanced interfacial compatibility and effective sodium dendrite growth suppression.

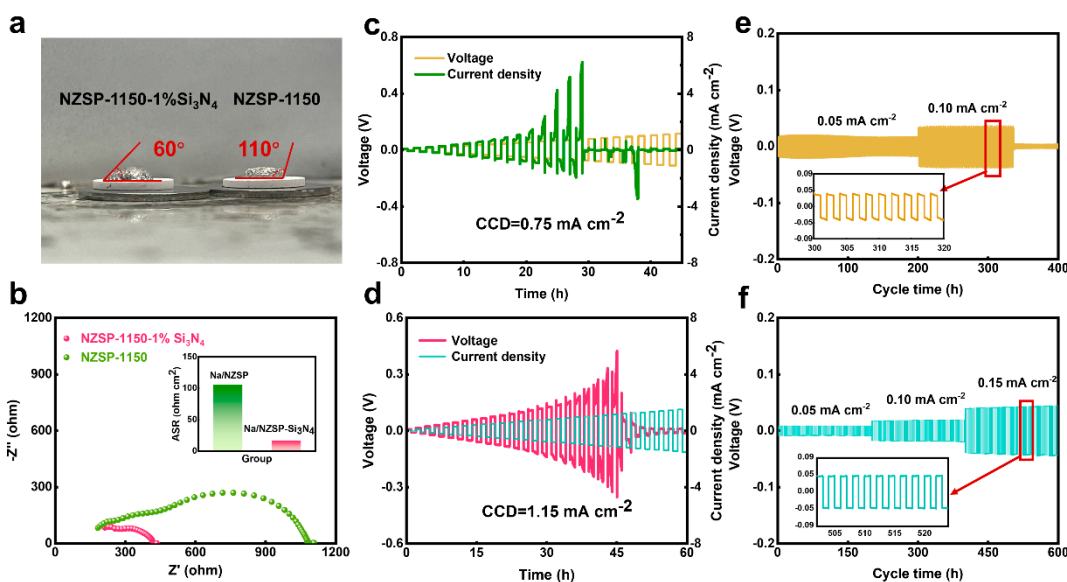


**Figure 3.** (a) Wettability test between NZSP-1150-1% $\text{Si}_3\text{N}_4$  electrolyte surface and Na metal. (b) The EIS plots of Na/NZSP-1150/Na and Na/NZSP-1150-1% $\text{Si}_3\text{N}_4$ /Na at room temperature. Critical current density (CCD) of (c) Na/NZSP-1150/Na and (d) Na/NZSP-1150-1% $\text{Si}_3\text{N}_4$ /Na. Room temperature voltage profiles of (e) Na/NZSP-1150/Na and (f) Na/NZSP-1150-1% $\text{Si}_3\text{N}_4$ /Na.

In order to investigate the electrode/electrolyte interface, the symmetrical cell with NZSP-1150-1% $\text{Si}_3\text{N}_4$  was disassembled after cycling. Subsequently, the surface of the ceramic electrolyte was subjected to XPS analysis. Figures 4a and S7 show the XPS analysis results of the ceramic electrolyte surface after cycling. It can be observed that the integrated area and relative intensity of the Na 1s peak increase after cycling, which is due to the increase in surface roughness and interface product coverage [32,33]. In addition, no notable changes are discerned in the spectra of Zr 3d, Si 2p, P 2p and N 1s. Figures 4b and S8 illustrate the superimposed SEM-EDS results of the cycled symmetric cell. It can demonstrate that the cycled ceramic electrolyte retains a considerable degree of microstructural density. There is no obvious “dead sodium” deposition phenomenon, and the electrolyte and sodium metal remain tightly combined, exhibiting no discernible voids between them. This indicates that the sodium metal uniformly deposited onto the ceramic electrolyte surface, with a highly intact interface. This is demonstrated in the mechanism diagram depicted in Figure 4c. Firstly, the pure-NZSP electrolyte has a loose microstructure and contains more voids, which increases the barrier to  $\text{Na}^+$  transfer and results in a non-uniform distribution of  $\text{Na}^+$  flux at the NZSP/Na interface, which is the main reason for the generation of dendrites at the interface. Furthermore, the unfavorable electronic conductivity of grain

boundaries in pure NZSP would facilitate the electrochemical reduction in  $\text{Na}^+$ , thereby promoting the nucleation and growth of metal dendrites [34–37]. Secondly, owing to the uneven Na-ion plating and stripping, there are inhomogeneous thermal distribution and hot spots within the ceramic electrolyte during battery cycling, where Na dendrites may be prone to grow [13,38]. Last, the poor wettability capability of the Na/NZSP surface indicates that the binding is unfavorable, making the entrapment of  $\text{Na}^+$  at the interface inhomogeneous, which results in the generation of voids or dendrites and ultimately leads to failure of the interfacial contact [39]. However, the addition of  $\text{Si}_3\text{N}_4$  can make the matrix structure denser while achieving lower electronic conductivity (Figure S9). In addition, due to the high thermal conductivity of  $\text{Si}_3\text{N}_4$ , it can conduct heat during battery cycling and effectively inhibit the generation of hot spots. On the other hand, due to the better interfacial wettability between Na metal and NZSP- $x\text{Si}_3\text{N}_4$ , the electrode/solid electrolyte bonding is tighter. Therefore, compared with pure NZSP, the NZSP- $x\text{Si}_3\text{N}_4$  electrolyte exhibits better electrochemical performance and interfacial compatibility.

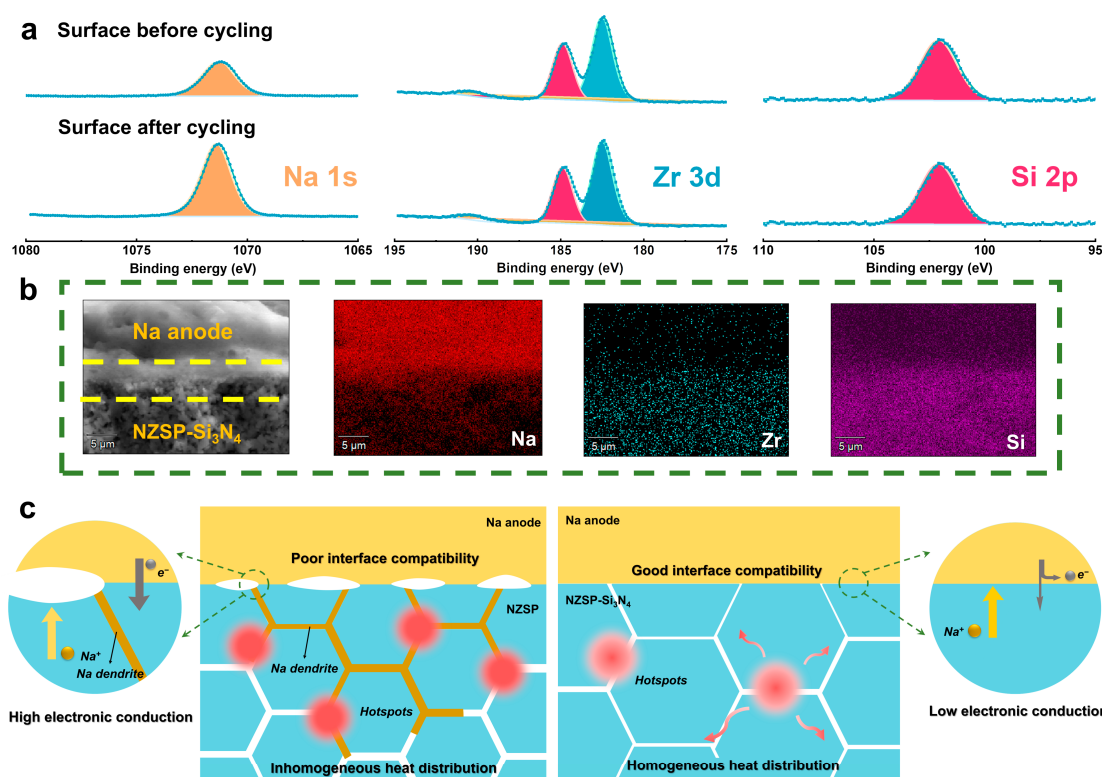


**Figure 4.** (a) XPS spectra of the NZSP-1150-1% $\text{Si}_3\text{N}_4$  surface before and after cycling. (b) Cross-sectional SEM image and corresponding EDS results of the cycled Na/NZSP-1150-1% $\text{Si}_3\text{N}_4$  interface. (c) Schematic illustration of NASICON-type electrolytes of NZSP (**left**) and NZSP- $\text{Si}_3\text{N}_4$  (**right**).

NZSP-1150-1% $\text{Si}_3\text{N}_4$  was utilized as the ceramic electrolyte to assemble solid-state sodium batteries, in which metallic sodium served as the anode and medium-entropy NASICON-structure  $\text{Na}_{3.5}\text{V}_{0.5}\text{Mn}_{0.5}\text{Fe}_{0.5}\text{Ti}_{0.5}(\text{PO}_4)_3$  (Me-NVMP) with high specific capacity was used for the cathode active substance [40]. Figure 5a presents the schematic diagram of the solid-state sodium metal cell and the resistance of the assembled battery at room temperature. It can be seen that the impedance of the solid-state battery using NZSP-1150-1% $\text{Si}_3\text{N}_4$  ceramic as the electrolyte at room temperature is much smaller than that of the solid-state battery using NZSP-1150 ceramic. The inset depicts the equivalent circuit, mainly composed of the solid electrolyte resistance and the interfacial resistance between the ceramic electrolyte and solid electrode. Figure 5b illustrates the rate performance of Na/NZSP-1150-1% $\text{Si}_3\text{N}_4$ /Me-NVMP, and Figure 5c exhibits the discharge/charge curves at different rates. The specific discharge capacities obtained are 154.1, 152.2 and 150.4 mAh

$\text{g}^{-1}$  at 1 C, 2 C and 3 C, respectively. The solid-state sodium batteries exhibit excellent rate performance when the rate is restored to 2 C and 1 C, with the discharge capacity recovered to 152.0 and 153.0  $\text{mAh g}^{-1}$ . Figure 5d,e show the electrochemical cycling performance and initial charge/discharge curves of Me-NVMP/NZSP-1150-1% $\text{Si}_3\text{N}_4$ /Na at 1 C. The first charge capacity is 152.7  $\text{mAh g}^{-1}$ , resulting in an initial Coulombic efficiency of 99.8%. After 200 cycles, the discharge capacity of the battery remains at 126.7  $\text{mA h g}^{-1}$  and a capacity retention of 82% is achieved. Meanwhile, the capacity of solid-state batteries with NZSP-1150 decays rapidly, and the capacity retention is 12%. Moreover, compared with other types of NSASICON electrolytes,  $\text{Si}_3\text{N}_4$ -doped NZSP ceramic electrolytes still exhibit better cycling performance in solid-state sodium metal batteries (Table S2). The results effectively demonstrate the feasibility of the utilization of NZSP- $x\text{Si}_3\text{N}_4$  electrolytes in solid-state sodium batteries.

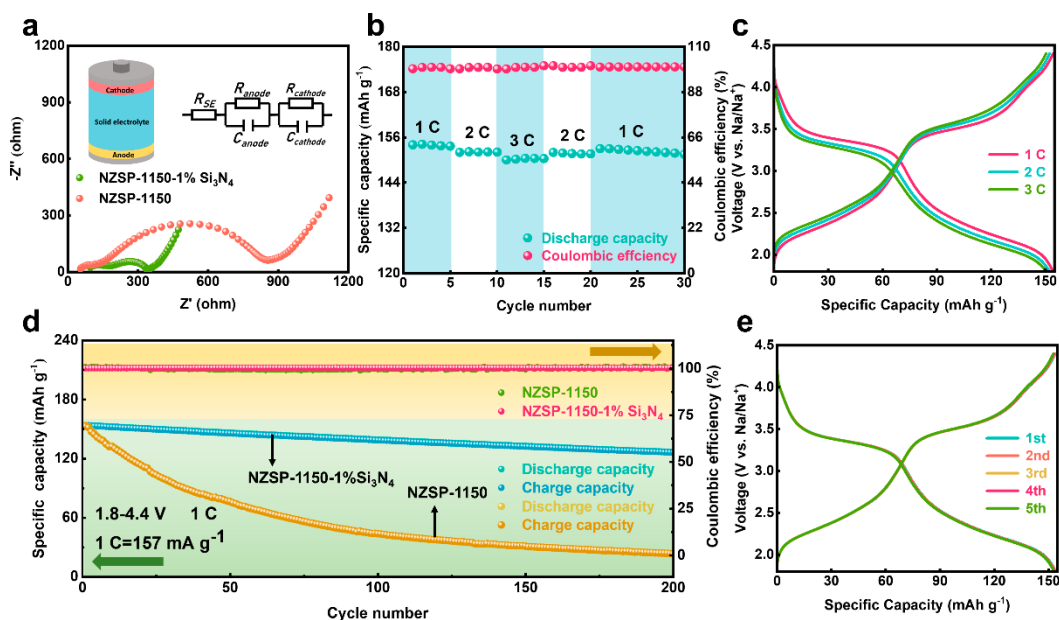


**Figure 5.** Electrochemical performance of solid-state sodium metal batteries based on NZSP-1150-1% $\text{Si}_3\text{N}_4$ . (a) EIS plots of the batteries. (b,c) Rate capability. (d) Cycling performance and (e) discharge/charge curves at 1 C.

#### 4. Conclusions

In our work, NZSP- $\text{Si}_3\text{N}_4$  ceramic was synthesized by a high-temperature solid-state reaction. The results illustrate that  $\text{Si}_3\text{N}_4$ , as a sintering additive, can effectively suppress the abnormal growth of grains and maintain uniform grain size, thereby promoting closer grain contact, achieving dense microstructure at a lower sintering temperature and higher room temperature ionic conductivity ( $3.82 \times 10^{-4} \text{ S cm}^{-1}$ ).  $\text{Si}_3\text{N}_4$  has high thermal conductivity and can inhibit the transmission of electrons between the electrolyte matrix grains, thus effectively hindering the generation of sodium metal dendrites. Moreover, because of the favorable wettability of the NZSP- $\text{Si}_3\text{N}_4$  against metallic Na electrode, the Na/NZSP-1150-1% $\text{Si}_3\text{N}_4$ /Na symmetric battery exhibits superior rate performance and cycling stability. Finally, good electrochemical performance is obtained via NASICON-based solid-state sodium metal batteries.

**Supplementary Materials:** The following supporting information can be downloaded at: <https://www.mdpi.com/article/10.3390/batteries10100359/s1>, Figure S1: XRD patterns of NZSP-1200- $x\text{Si}_3\text{N}_4$ . Figure S2: cross-sectional SEM images of NZSP-1200. Figure S3: electrochemical impedance spectra of NZSP-1200- $x\text{Si}_3\text{N}_4$ . Figure S4: Nyquist plot of NZSP-1150-1% $\text{Si}_3\text{N}_4$  at room temperature, simulation result based on the equivalent circuit, and illustration of analysis of  $R_b$  and  $R_{gb}$ . Table S1: ionic conductivity ( $\sigma$ ) of NZSP-1150- $x\text{Si}_3\text{N}_4$  and NZSP-1200- $x\text{Si}_3\text{N}_4$ . Figure S5: Nyquist

plots variation with temperature of NZSP-1200, the inset shows the temperature-dependent Arrhenius plots. Figure S6: room temperature Nyquist plots of symmetric sodium metal batteries based on (a) NZSP-1150-1% $\text{Si}_3\text{N}_4$  and (b) NZSP-1150 ceramic electrolytes. The insets are the equivalent circuit and illustration of analysis of  $R_{\text{SE}}$  and  $R_{\text{t}}$ . Figure S7: XPS spectra of the NZSP-1150-1% $\text{Si}_3\text{N}_4$  ceramic electrolyte surface before and after cycling. Figure S8: cross-sectional EDS mapping results of O and N elements of the cycled NZSP-1150-1% $\text{Si}_3\text{N}_4$  interface. Figure S9: cross-sectional EDS mapping results of the NZSP-1150-7% $\text{Si}_3\text{N}_4$ . Figure S10: DC polarization plots of NZSP-1150-1% $\text{Si}_3\text{N}_4$  and NZSP-1150. Table S2: comparison of the cycling performance of different types of electrolytes in all-solid-state batteries at room temperature [22,41–43].

**Author Contributions:** Conceptualization, Y.Z.; Formal analysis, W.S., Y.L., C.S. and Z.S.; Funding acquisition, Y.Z.; Investigation, H.J. and Y.Z.; Methodology, W.S., Y.L., C.S. and Z.S.; Project administration, H.J. and Y.Z.; Software, W.S.; Validation, W.S.; Writing—original draft, W.S.; Writing—review and editing, Y.Z. All authors have read and agreed to the published version of the manuscript.

**Funding:** Y.Z. acknowledges funding support from the open research fund of Songshan Lake Materials Laboratory (No. 2022SLABFN24), the National Natural Science Foundation of China (No. 52072033), and the State Key Laboratory of New Ceramic and Fine Processing Tsinghua University (No. 202211).

**Data Availability Statement:** The data presented in this study are available upon request from the corresponding author.

**Conflicts of Interest:** The authors declare no conflicts of interest.

## References

1. Goodenough, J. Electrochemical energy storage in a sustainable modern society. *Energy Environ. Sci.* **2014**, *7*, 14–18. [[CrossRef](#)]
2. Kim, T.-H.; Park, J.-S.; Chang, S.K.; Choi, S.; Ryu, J.H.; Song, H.-K. The current move of lithium ion batteries towards the next phase. *Adv. Energy Mater.* **2012**, *2*, 860–872. [[CrossRef](#)]
3. Chayambuka, K.; Mulder, G.; Danilov, D.L.; Notten, P.H.L. From Li-ion batteries toward Na-ion chemistries: Challenges and opportunities. *Adv. Energy Mater.* **2020**, *10*, 1–11. [[CrossRef](#)]
4. Hwang, J.-Y.; Myung, S.-T.; Sun, Y.-K. Sodium-ion batteries: Present and future. *Chem. Soc. Rev.* **2017**, *46*, 3529–3614. [[CrossRef](#)]
5. Kim, S.-W.; Seo, D.-H.; Ma, X.; Ceder, G.; Kang, K. Electrode materials for rechargeable sodium-ion batteries: Potential alternatives to current lithium-ion batteries. *Adv. Energy Mater.* **2012**, *2*, 710–721. [[CrossRef](#)]
6. Palomares, V.; Serras, P.; Villaluenga, I.; Hueso, K.B.; Carretero-González, J.; Rojo, T. Na-ion batteries, recent advances and present challenges to become low cost energy storage systems. *Energy Environ. Sci.* **2012**, *5*, 5884–5901. [[CrossRef](#)]
7. Wang, L.G.; Li, J.; Lu, G.L.; Li, W.Y.; Tao, Q.Q.; Shi, C.H.; Huile, J.; Chen, G.; Wang, S. Fundamentals of electrolytes for solid-state batteries: Challenges and perspectives. *Front. Mater.* **2020**, *7*, 111. [[CrossRef](#)]
8. Li, Y.; Li, M.; Sun, Z.; Ni, Q.; Jin, H.B.; Zhao, Y.J. Recent advance on NASICON electrolyte in solid-state sodium metal batteries. *Energy Storage Mater.* **2023**, *56*, 582–599. [[CrossRef](#)]
9. Krok, F. Influence of sintering conditions on chemical composition of NASICON. *Solid State Ion.* **1987**, *24*, 21–28. [[CrossRef](#)]
10. Dai, H.Q.; Chen, Y.Y.; Xu, W.Q.; Hu, Z.; Gu, J.; Wei, X.; Xie, F.X.; Zhang, W.L.; Wei, W.; Guo, R.Q.; et al. A review of modification methods of solid electrolytes for all-solid-state sodium-ion batteries. *Energy Technol.* **2021**, *9*, 1–13. [[CrossRef](#)]
11. Zhao, C.L.; Liu, L.; Qi, X.G.; Lu, Y.X.; Wu, F.X.; Zhao, J.M.; Yu, Y.; Hu, Y.-S.; Chen, L.Q. Solid-state sodium batteries. *Adv. Energy Mater.* **2018**, *8*, 1–20. [[CrossRef](#)]
12. Ma, Q.L.; Tietz, F. Solid-state electrolyte materials for sodium batteries: Towards practical applications. *ChemElectroChem* **2020**, *7*, 2693–2713. [[CrossRef](#)]
13. Zhu, Y.Y.; Xie, J.; Pei, A.L.; Liu, B.F.; Wu, Y.C.; Lin, D.C.; Li, J.; Wang, H.S.; Chen, H.; Xu, J.W.; et al. Fast lithium growth and short circuit induced by localized-temperature hotspots in lithium batteries. *Nat. Commun.* **2019**, *10*, 2067. [[CrossRef](#)] [[PubMed](#)]
14. Shen, Q.; Lin, Z.J.; Deng, J.J.; Chen, H.X.; Chen, X.; Tian, J.; Bao, B.L.; Dai, P.Q.; Sun, X.D. Effects of  $\beta$ - $\text{Si}_3\text{N}_4$  seeds on microstructure and performance of  $\text{Si}_3\text{N}_4$  ceramics in semiconductor package. *Materials* **2023**, *16*, 4461. [[CrossRef](#)]
15. Lukianova, O.A.; Khmara, A.N.; Perevislov, S.N.; Kolesnikov, D.A.; Krasilnikov, V.V. Electrical resistivity of silicon nitride produced by various methods. *Ceram. Int.* **2019**, *45*, 9497–9501. [[CrossRef](#)]
16. Jiang, Q.-G.; Guo, W.-M.; Liu, W.; Gu, S.-X.; Cheng, L.-X.; Liu, J.; Zhou, M.-P.; Wu, S.-H. Influence of powder characteristics on hot-pressed  $\text{Si}_3\text{N}_4$ . *Ceramics. Sci. Sinter.* **2017**, *49*, 81–89. [[CrossRef](#)]
17. Xing, H.Y.; Liu, B.Q.; Sun, J.; Zou, B. Mechanical properties of  $\text{Si}_3\text{N}_4$  ceramics from an in-situ synthesized  $\alpha$ - $\text{Si}_3\text{N}_4$ / $\beta$ - $\text{Si}_3\text{N}_4$  composite powder. *Ceram. Int.* **2017**, *43*, 2150–2154. [[CrossRef](#)]
18. Pearson, R.G. Bond energies, force constants and electronegativities. *J. Mol. Struct.* **1993**, *300*, 519–525. [[CrossRef](#)]
19. Bickmore, B.R.; Craven, O.; Wander, M.C.F.; Checketts, H.; Whitmer, J.; Shurtleff, C.; Yeates, D.; Ernstrom, K.; Andros, C.; Thompson, H. Bond valence and bond energy. *Am. Mineral.* **2017**, *102*, 804–812. [[CrossRef](#)]

20. Qteish, A. Electronegativity scales and electronegativity-bond ionicity relations: A comparative study. *J. Phys. Chem. Solids* **2019**, *124*, 186–191. [[CrossRef](#)]
21. Fuentes, R.O.; Figueiredo, F.L.; Marques, F.M.B.; Franco, J.I. Processing and electrical properties of NASICON prepared from yttria-doped zirconia precursors. *J. Eur. Ceram. Soc.* **2001**, *21*, 737–743. [[CrossRef](#)]
22. Li, Y.; Sun, Z.; Jin, H.B.; Zhao, Y.J. Engineered grain boundary enables the room temperature solid-state sodium metal batteries. *Batteries* **2023**, *9*, 252. [[CrossRef](#)]
23. Zheng, C.J.; Lu, Y.; Su, J.M.; Song, Z.; Xiu, T.P.; Jin, J.; Badding, M.E.; Wen, Z.Y. Grain boundary engineering enabled high-performance garnet-type electrolyte for lithium dendrite free lithium metal batteries. *Small Methods* **2022**, *6*, e2200667. [[CrossRef](#)] [[PubMed](#)]
24. Zhao, X.C.; Luo, Y.S.; Zhao, X.J. Effect of  $\text{TeO}_2$  sintering aid on the microstructure and electrical properties of  $\text{Li}_{1.3}\text{Al}_{0.3}\text{Ti}_{1.7}(\text{PO}_4)_3$  solid electrolyte. *J. Alloys Compd.* **2022**, *927*, 167019. [[CrossRef](#)]
25. Thokchom, J.S.; Kumar, B. The effects of crystallization parameters on the ionic conductivity of a lithium aluminum germanium phosphate glass-ceramic. *J. Power Sources* **2010**, *195*, 2870–2876. [[CrossRef](#)]
26. Naqash, S.; Ma, Q.L.; Tietz, F.; Guillon, O.  $\text{Na}_3\text{Zr}_2(\text{SiO}_4)_2(\text{PO}_4)$  prepared by a solution-assisted solid state reaction. *Solid State Ion.* **2017**, *302*, 83–91. [[CrossRef](#)]
27. Shao, Y.J.; Zhong, G.M.; Lu, Y.X.; Liu, L.L.; Zhao, C.L.; Zhang, Q.Q.; Hu, Y.-S.; Yang, Y.; Chen, L.Q. A novel NASICON-based glass-ceramic composite electrolyte with enhanced Na-ion conductivity. *Energy Storage Mater.* **2019**, *23*, 514–521. [[CrossRef](#)]
28. He, S.S.; Xu, Y.L.; Chen, Y.J.; Ma, X.N. Enhanced ionic conductivity of an  $\text{F}^-$ -assisted  $\text{Na}_3\text{Zr}_2\text{Si}_2\text{PO}_{12}$  solid electrolyte for solid-state sodium batteries. *J. Mater. Chem. A* **2020**, *8*, 12594–12602. [[CrossRef](#)]
29. Park, H.; Jung, K.; Nezafati, M.; Kim, C.-S.; Kang, B. Sodium ion diffusion in NASICON ( $\text{Na}_3\text{Zr}_2\text{Si}_2\text{PO}_{12}$ ) solid electrolytes: Effects of excess sodium. *ACS Appl. Mater. Interfaces* **2016**, *8*, 27814–27824. [[CrossRef](#)]
30. Wu, B.B.; Wang, S.Y.; Lochala, J.; Desrochers, D.; Liu, B.; Zhang, W.Q.; Yang, J.H.; Xiao, J. The role of the solid electrolyte interphase layer in preventing Li dendrite growth in solid-state batteries. *Energy Environ. Sci.* **2018**, *11*, 1803–1810. [[CrossRef](#)]
31. Ning, Z.Y.; Jolly, D.S.; Li, G.C.; Meyere, R.D.; Pu, S.D.; Chen, Y.; Kasemchainan, J.; Ihli, J.; Gong, C.; Liu, B.Y.; et al. Visualizing plating-induced cracking in lithium-anode solid-electrolyte cells. *Nat. Mater.* **2021**, *20*, 1121–1129. [[CrossRef](#)] [[PubMed](#)]
32. Zhang, Z.Z.; Wenzel, S.; Zhu, Y.Z.; Sann, J.; Shen, L.; Yang, J.; Yao, X.Y.; Hu, Y.-S.; Wolverton, C.; Li, H.; et al.  $\text{Na}_3\text{Zr}_2\text{Si}_2\text{PO}_{12}$ : A stable  $\text{Na}^+$ -ion solid electrolyte for solid-state batteries. *ACS Appl. Energy Mater.* **2020**, *3*, 7427–7437. [[CrossRef](#)]
33. Sun, Z.; Zhao, Y.J.; Ni, Q.; Liu, Y.; Sun, C.; Li, J.; Jin, H.B. Solid-state Na metal batteries with superior cycling stability enabled by ferroelectric enhanced Na/ $\text{Na}_3\text{Zr}_2\text{Si}_2\text{PO}_{12}$  interface. *Small* **2022**, *18*, 2200716. [[CrossRef](#)]
34. Sun, C.; Zhao, Y.J.; Ni, Q.; Sun, Z.; Yuan, X.Y.; Li, J.B.; Jin, H.B. Reversible multielectron redox in NASICON cathode with high energy density for low-temperature sodium-ion batteries. *Energy Storage Mater.* **2022**, *49*, 291–298. [[CrossRef](#)]
35. Oh, J.A.S.; He, L.; Chua, B.; Zeng, K.; Lu, L. Inorganic sodium solid-state electrolyte and interface with sodium metal for room-temperature metal solid-state batteries. *Energy Storage Mater.* **2021**, *34*, 28–44. [[CrossRef](#)]
36. Wang, X.X.; Chen, J.J.; Mao, Z.Y.; Wang, D.J. Effective resistance to dendrite growth of NASICON solid electrolyte with lower electronic conductivity. *Chem. Eng. J.* **2022**, *427*, 130899. [[CrossRef](#)]
37. Ruan, Y.L.; Guo, F.; Liu, J.J.; Song, S.D.; Jiang, N.Y.; Cheng, B.W. Optimization of  $\text{Na}_3\text{Zr}_2\text{Si}_2\text{PO}_{12}$  ceramic electrolyte and interface for high performance solid-state sodium battery. *Ceram. Int.* **2019**, *45*, 1770–1776. [[CrossRef](#)]
38. Zhang, C.; Hu, X.C.; Nie, Z.W.; Wu, C.; Zheng, N.; Chen, S.J.; Yang, Y.H.; Wei, R.; Yu, J.M.; Yang, N.; et al. High-performance Ta-doped  $\text{Li}_7\text{La}_3\text{Zr}_2\text{O}_{12}$  garnet oxides with AlN additive. *J. Adv. Ceram.* **2022**, *11*, 1530–1541. [[CrossRef](#)]
39. Li, Y.; Sun, Z.; Yuan, X.Y.; Jin, H.B.; Zhao, Y.J. NaBr-assisted sintering of  $\text{Na}_3\text{Zr}_2\text{Si}_2\text{PO}_{12}$  ceramic electrolyte stabilizes a rechargeable solid-state sodium metal battery. *ACS Appl. Mater. Interfaces* **2023**, *15*, 49321–49328. [[CrossRef](#)]
40. Li, M.; Sun, C.; Yuan, X.Y.; Li, Y.; Yuan, Y.F.; Jin, H.B.; Lu, J.; Zhao, Y.J. A configuration entropy enabled high performance polyanionic cathode for sodium-ion batteries. *Adv. Funct. Mater.* **2024**, *34*, 1–10. [[CrossRef](#)]
41. Zhao, Y.J.; Wang, C.Z.; Dai, Y.J.; Jin, H.B. Homogeneous  $\text{Na}^+$  transfer dynamic at Na/ $\text{Na}_3\text{Zr}_2\text{Si}_2\text{PO}_{12}$  interface for all solid-state sodium metal batteries. *Nano Energy* **2021**, *88*, 106293. [[CrossRef](#)]
42. Miao, X.; Di, H.; Ge, X.; Zhao, D.; Wang, P.; Wang, R.; Wang, C.; Yin, L.  $\text{AlF}_3$ -modified anode-electrolyte interface for effective Na dendrites restriction in NASICON-based solid-state electrolyte. *Energy Storage Mater.* **2020**, *30*, 170–178. [[CrossRef](#)]
43. Wang, X.; Liu, Z.; Tang, Y.; Chen, J.; Wang, D.; Mao, Z. Low temperature and rapid microwave sintering of  $\text{Na}_3\text{Zr}_2\text{Si}_2\text{PO}_{12}$  solid electrolytes for Na-ion batteries. *J. Power Sources* **2021**, *481*, 228924. [[CrossRef](#)]

**Disclaimer/Publisher’s Note:** The statements, opinions and data contained in all publications are solely those of the individual author(s) and contributor(s) and not of MDPI and/or the editor(s). MDPI and/or the editor(s) disclaim responsibility for any injury to people or property resulting from any ideas, methods, instructions or products referred to in the content.